Phases of ^{4}He and H$_2$ adsorbed on a single carbon nanotube

M. C. Gordillo ⬤

Departamento de Sistemas Físicos, Químicos y Naturales, Universidad Pablo de Olavide, Carretera de Utrera km 1, E-41013 Sevilla, Spain
and Instituto Carlos I de Física Terica y Computacional, Universidad de Granada, E-18071 Granada, Spain

R. Rodríguez-García

Departamento de Sistemas Físicos, Químicos y Naturales, Universidad Pablo de Olavide, Carretera de Utrera km 1, E-41013 Sevilla, Spain

J. Boronat ⬤

Departament de Física, Universitat Politècnica de Catalunya, Campus Nord B4-B5, E-08034 Barcelona, Spain

Using a diffusion Monte Carlo technique, we calculated the phase diagrams of ^{4}He and H$_2$ adsorbed on a single (5,5) carbon nanotube, one of the narrowest that can be obtained experimentally. For a single monolayer, when the adsorbate density increases, both species undergo a series of first-order solid-solid phase transitions between incommensurate arrangements. Remarkably, the ^{4}He lowest-density solid phase shows supersolid behavior, in contrast to the normal solid that we found for H$_2$. The nature of the second layer is also different for both adsorbates. Contrary to what happens on graphite, the second layer of ^{4}He on the tube is a liquid, at least up to the density corresponding to a third-layer promotion on a flat substrate. However, the second layer of H$_2$ is a solid that, at its lowest stable density, has a small, but observable, superfluid fraction.

I. INTRODUCTION

A carbon nanotube can be thought of as being the result of folding a single graphene sheet over itself to form a seamless cylinder [1]. It is then a quasi-one-dimensional structure that can be coated with different kinds of adsorbates. In principle, that reduced dimensionality could produce phase diagrams different from those on quasi-two-dimensional environments such as graphite or graphene. Studying the adsorption capabilities of those carbon cylinders is possible since an isolated carbon nanotube can be synthesized and made to work as a mechanical resonator. Its resonant frequencies change upon loading, allowing in this way an accurate determination of the adsorbate phases [2–8]. In principle, this resonant frequency can be monitored to check whether we have a supersolid structure, as was done for the second layer of ^{4}He on graphite [9,10].

Experimental studies on Ne, Ar, and Kr [2,3,6] indicate that the first layers of those gases on nanotubes are qualitatively similar to those found in their flat equivalents, the only difference being the smaller binding energies in the cylinders due to their curved nature [2,3]. On the other hand, it is known that ^{4}He on a single nanotube is adsorbed in a layer-by-layer process, similar to deposition on graphite [7]. The main goal of our present work is to deeply study the behavior of ^{4}He and H$_2$ on top of a (5,5) carbon nanotube in both the first and second layers. We chose this tube since its narrowness, with a radius of 3.42 Å, makes any difference from a flat graphite (or graphene) substrate larger than for thicker tubes. In particular, we were interested in studying whether the imposed curvature produced any additional phase, such as the supersolids experimentally detected [9–11] and theoretically

predicted in the first [12] and second layers of ^{4}He on a carbon substrate [13] and in the second layer of H$_2$ on graphite [14]. That superfluidity in first-layer solids was not calculated in previous studies [15,16]. We also explored the possibility of second-layer liquid phases for both species.

The rest of this paper is organized as follows. The diffusion Monte Carlo method used in our study is discussed in Sec. II. Section III contains the results obtained, with special attention given to the stable phases of both ^{4}He and H$_2$ adsorbed on the nanotube. The results for the superfluid fraction were calculated using the standard winding number estimator in the limit of zero temperature. Finally, the main conclusions and discussion of the results are given in Sec. IV.

II. METHOD

To study the stability of the different phases, we calculated the respective ground states ($T = 0$) of ^{4}He atoms and H$_2$ molecules on a corrugated carbon nanotube at several densities. This means writing down and solving the many-body Schrödinger equation that describes the adsorbate. Following previous works on similar systems, the Hamiltonian can be written down as

$$H = \sum_{i=1}^{N} \left[-\frac{\hbar^2}{2m} \nabla_i^2 + V_{\text{ext}}(x_i, y_i, z_i) \right] + \sum_{i<j}^{N} V_{\text{pair}}(r_{ij}), \quad (1)$$

where x_i, y_i, and z_i are the coordinates of each of the N adsorbate particles with mass m. $V_{\text{ext}}(x_i, y_i, z_i)$ is the interaction potential between each atom or molecule and all the individual carbon atoms in the nanotube, which is considered to be a rigid structure. Those potentials are of Lennard-Jones type,

with standard parameters taken from Ref. [17] in the case of ^{4}He-C interaction and from Ref. [18] for the H$_2$-C interaction. V_{pair} accounts for the ^{4}He-^{4}He and H$_2$-H$_2$ interactions (the Aziz and Wong [19] and Silvera and Goldman [20] potentials, respectively), which depend only on the distance r_{ij} between particles i and j. Both potentials are the standard models in previous studies.

To actually solve the many-body Schrödinger equation derived from the Hamiltonian in Eq. (1), we resorted to the diffusion Monte Carlo (DMC) algorithm. This stochastic numerical technique obtains, within some statistical noise, relevant ground-state properties of the N-particle system. To guide the diffusion process involved in DMC, one introduces a trial wave function that guides the importance sampling, reducing the variance to a manageable level. The trial wave functions used in our work derive from similar forms used previously in DMC calculations of ^{4}He and H$_2$ on graphene and graphite [13,14,21,22] that were able to reproduce available experimental data [9,10,23–27]. We are then confident that the trial wave functions used in the present work will also provide a reasonable description of the adsorbates on a similar, albeit curved, substrate.

In the present case, the trial wave function was built as a product of two terms. The first one is of Jastrow type between the adsorbate particles,

$$\Phi_J(\mathbf{r}_1, \ldots, \mathbf{r}_N) = \prod_{i<j}^{N} \exp\left[-\frac{1}{2}\left(\frac{b}{r_{ij}}\right)^5 \right], \qquad (2)$$

with b being a variationally optimized parameter whose values were 3.07 Å for the ^{4}He-^{4}He case [15] and 3.195 Å for the H$_2$-H$_2$ pair [16]. The second part incorporates the presence of the C atoms and localization terms,

$$\begin{aligned}
\Phi_s(\mathbf{r}_1, \ldots, \mathbf{r}_N) = & \prod_{i}^{N} \prod_{J}^{N_C} \exp\left[-\frac{1}{2}\left(\frac{b_{\text{C}}}{r_{iJ}}\right)^5 \right] \\
& \times \prod_{I=1}^{N} \left[\sum_{i=1}^{N} \exp\{-c_{1,2}[(\mathbf{r}_i - \mathbf{r}_{\text{site},I})^2]\} \right] \\
& \times \prod_{i}^{N} \Psi(R_i).
\end{aligned} \qquad (3)$$

Here, N_C stands for the number of carbon atoms of the nanotube, while the parameters b_C were taken from previous calculations for the same substrates [15,16]. r_{iJ} are the distances between a particle i (^{4}He or H$_2$) and a carbon atom J. $\Psi(R_i)$ is a one-body function that depends on the radial distance of those particles to the central axis of the tube R_i. For an atom or molecule located on the layer closest to the carbon substrate, those $\Psi(R_i)$'s were taken from Refs. [15,16] for ^{4}He and H$_2$. Those functions have maxima located at distances from the center of 6.26 and 6.36 Å, respectively. On the other hand, following the procedure already used for graphite [13,14,28], we radially confined particles in the second layer by Gaussian functions with variationally optimized parameters.

The remaining part of Eq. (3) allows us to distinguish between a translationally invariant liquid ($c_{1,2} = 0$) and a (super)solid phase ($c_{1,2} \neq 0$). Labels 1 and 2 stand for the first and second layers, respectively. For solids, the values of $c_{1,2}$ were variationally optimized to obtain the minimum energies for each species and density. For particles in the first layer, the parameters for the solid were found to be identical to those obtained for flat graphene and used in previous calculations for similar systems [15,16]. This means we used linear extrapolations between $c_1 = 0.15$ Å^{-2} (for a density of 0.08 Å^{-2}) and $c_1 = 0.77$ Å^{-2} (for 0.1 Å^{-2}) for ^{4}He [21] and between $c_1 = 0.61$ Å^{-2} (for 0.08 Å^{-2}) and $c_1 = 1.38$ Å^{-2} (for 0.1 Å^{-2}) in the case of H$_2$ [22]. For lower densities we used the value corresponding to 0.08 Å^{-2}, and for larger ones, the one corresponding to 0.1 Å^{-2}. For the second layer of H$_2$, $c_2 = 0.46$ Å^{-2} was used for all densities. The optimal c_2 parameter for ^{4}He was $c_2 = 0$, which corresponds to a liquid (see below). For any value of $c_{1,2}$, the form of the trial function allows the ^{4}He atoms and the H$_2$ molecules to be involved in exchanges and recovering indistinguishability, a necessary ingredient for modeling a supersolid [12]. Alternatively, for solid phases one can use a simplified version of Eq. (3) in which each particle is pinned to a single crystallographic site. This is the ansatz used to describe first-layer phases in Refs. [15,16] and will produce, by construction, normal solids. When we used that approximation, we obtained energies per particle that were higher than or equal to those we obtained when we used Eq. (3). The case with equal values for the energies corresponds to situations in which the superfluid estimator is equal to zero, i.e., when we recover the normal behavior of the solid.

Finally, in Eq. (3), x_{site}, y_{site}, and z_{site} are the crystallographic positions that define the solids we wrap around the (5,5) tube. Those are incommensurate arrangements built up by locating a given number n of adsorbate particles on planes perpendicular to the main axis of the nanotube. One can visualize those phases by imagining that the coated cylinder is cut longitudinally to have a long rectangle in which the shorter side corresponds to the length of the circumference that defines the tube. In the case of the first ^{4}He layer, this means $2\pi \times 6.26$ Å (see above). On that short side, we locate n uniformly spaced atoms or molecules, with a distance between them in the transverse (short) direction of d_t (Å), and add as many parallel rows as the length of the tube will allow. Those arrays of atoms will be separated by a longitudinal distance of d_l (Å). Between those rows, we will include another one separated by $d_l/2$ from the contiguous lines, whose particles will be displaced $d_t/2$ in the transverse direction with respect to the previous and following lines. A similar procedure is used to build the solids in the second layer, located at average distances for the center or the tube of 8.98 and 9.42 Å for ^{4}He and H$_2$, respectively. Since we started with n particles located on rows in the transverse direction, following Refs. [15,16], we call these phases n-in-a-row solids. A picture of one of those phases can be found in Ref. [16] for the case of H$_2$.

The data presented in this paper are the mean of 10 independent DMC simulations, and the error bars, when shown, correspond to the variance of these calculations. Every DMC history consists of 1.2×10^5 steps involving a movement of all the particles of each of the 300 replicas (walkers) that describe the different configurations. Larger numbers of walkers or longer simulations do not change the averages given. The values of the observables presented here were calculated
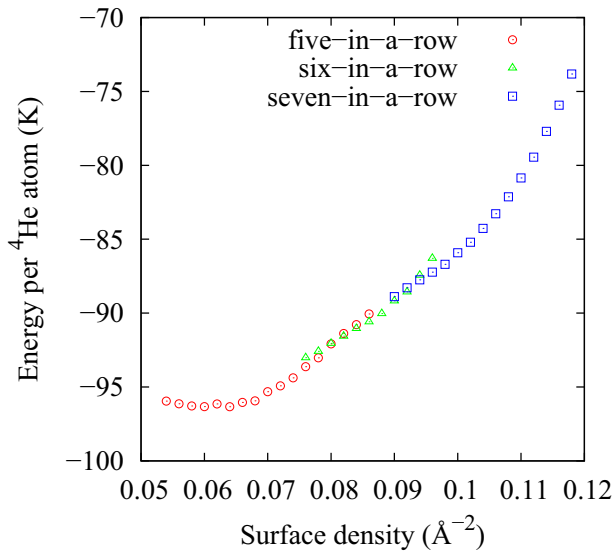
FIG. 1. Energy per ^{4}He atom as a function of the density for n-in-a-row ($n = 5, 6, 7$) first-layer solids.

TABLE I. Lowest and highest stability density limits for the different single-layer solid phases adsorbed on a (5,5) carbon nanotube. We include also the lowest stable density limit for the second layer of ^{4}He, a liquid, and of H$_2$, a solid. The error bars are given in parentheses and correspond to the last decimal place given.

^{4}He		H$_2$	
ρ (Å^{-2})	E (K)	ρ (Å^{-2})	E (K)
5-in-a row			
0.0605(5)	−96.5(1)	0.062(2)	−349.0(1)
0.076(1)	−93.7(1)	0.068(2)	−346.1(1)
6-in-a-row			
0.086(2)	−90.6(1)	0.080(2)	−334.1(1)
0.088(1)	−90.0(1)	0.085(2)	−326.7(1)
7-in-a-row			
0.096(2)	−87.2(1)	0.0925(5)	−314.3(1)
0.110(2)	−80.9(1)	0.0975(5)	−304.1(1)
Second layer			
0.181(1)	−48.9(1)	0.166(2)	−199.7(1)

after equilibration (2×10^4 time steps), i.e., when no obvious drift in their values as a function of the simulation time was detected. We made the simulations on isolated tubes, which means that periodic boundary conditions were applied only in the direction corresponding to the length of the tube. The number of particles in the simulation cells and their lengths were varied to produce the desired densities for either of the two adsorbates. The first number was between a minimum of 100 (for a one-layer tube) and a maximum of 364 for the highest densities considered in this work. However, some simulations including up to 500 particles were made to verify that our results were not affected by size effects. Conversely, the lengths of the simulation cells varied in the range of 33–45 Å.

III. RESULTS

A. ^{4}He

We first study the phase diagram of ^{4}He on a (5,5) nanotube, including the promotion from the first to a second layer. Figure 1 gives us the energy per particle for the different first-layer incommensurate solids. Those extend the results given in Ref. [15] in two ways. First, we consider now larger helium densities in the 7-in-a-row solid, which allows us to study all the possible first-order transitions between incommensurate arrangements up to the second-layer promotion. In addition, since those first-layer solids are described by Eq. (3), instead of having each particle of the solid pinned to a single crystallographic position (Nosanow-Jastrow wave function), we can access any possible supersolid phases.

The energies per particle for the three n-in-a-row ^{4}He ($n = 5, 6, 7$) solids are shown in Fig. 1. As indicated above, to calculate the surface densities we used cylinders with the radius given by the average distance from the ^{4}He atoms to the center of the tube, in this case 6.26 Å. We do not show in Fig. 1 the results of a translationally invariant liquid phase because the energies for that phase are above the ones displayed. The same applies for the 2/5, 3/7, and $\sqrt{3} \times \sqrt{3}$ registered solids

[26]. By means of a least-squares fit to the 5-in-a-row data, we can obtain the minimum density and its corresponding energy per particle. The results are given in Table I. There, we can see that they are slightly different from those of Ref. [15], with $\rho = 0.062$ Å^{-2} and $E = -96.10$ K. The reason for the discrepancy is that the 5-in-a-row solid is a supersolid instead of the normal solid previously considered. Its superfluid density was calculated using the zero-temperature winding number estimator derived in Ref. [29],

$$\frac{\rho_s}{\rho} = \lim_{\tau \to \infty} \alpha \left(\frac{D_s(\tau)}{\tau} \right), \tag{4}$$

with τ being the imaginary time used in the quantum Monte Carlo simulation. Here, $\alpha = N/(2D_0)$, with $D_0 = \hbar^2/(2m)$ and $D_s(\tau) = \langle [\mathbf{R}_{c.m.}(\tau) - \mathbf{R}_{c.m.}(0)]^2 \rangle$. $\mathbf{R}_{c.m.}$ is the position of the center of mass of the N ^{4}He atoms in the simulation box, using only their z coordinates on which periodic boundary conditions are applied.

The results of the superfluid estimator for the 5-in-a-row solid are given in Fig. 2 for $\rho = 0.062$ Å^{-2} (solid squares) and 0.064 Å^{-2} (open squares). The line is a least-squares fit to $\alpha D_s(\tau)$ versus τ for the lowest density in the range $3 < \tau < 8$ K^{-1}. The value obtained is $\rho_s/\rho = 1.31\% \pm 0.05\%$ for 0.062 Å^{-2} and $\rho_s/\rho = 1.35\% \pm 0.05\%$ (line not shown) for 0.064 Å^{-2}. In both cases, the superfluid fraction is of the same order, but slightly larger, than the one found for a registered phase of $\rho = 0.0636$ Å^{-2} for ^{4}He on graphene ($\rho_s/\rho = 0.67\% \pm 0.01\%$) [12]. No significant size effects were found for larger simulation cells, in accordance with results in Ref. [14].

Using the data reported in Fig. 1 and by means of double-tangent Maxwell constructions, we can obtain the stability limits of the different first-layer ^{4}He solid phases. The results are given in Table I, where we provide the lowest and highest stable densities ρ for those arrangements. This means that, for instance, there is a first-order phase transition between a 5-in-a-row solid with $\rho = 0.076$ Å^{-2} and a 6-in-a-row one with $\rho = 0.086$ Å^{-2}, and the same can be said for a 6-in-a-row
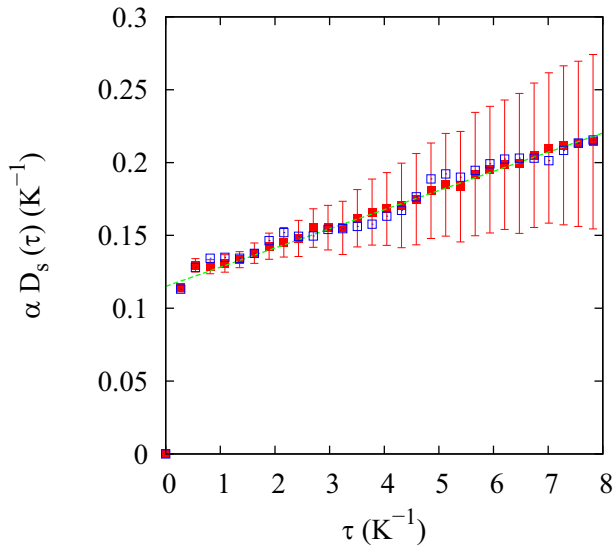
FIG. 2. Estimator of the superfluid density for the first-layer 5-in-a-row supersolid ^{4}He phase at $\rho = 0.062$ Å^{-2} (solid squares) and $\rho = 0.062$ Å^{-2} (open squares). The straight line is a linear least-squares fit to the $\rho = 0.062$ Å^{-2} data for $\tau > 3$ K^{-1}.

structure with $\rho = 0.088$ Å^{-2} and a 7-in-a-row structure with $\rho = 0.096$ Å^{-2}. Both 6- and 7-in-a-row solids are normal solids, with $\rho_s/\rho = 0$.

If we keep increasing the ^{4}He density on top of the nanotube, it is promoted to a second layer. To obtain the stability range of that second layer, we used the same technique as in
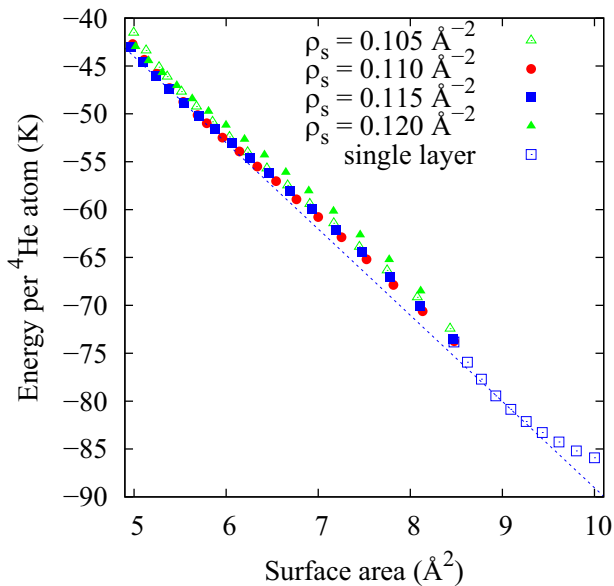
FIG. 3. Energy per ^{4}He atoms as a function of the inverse of the total ^{4}He density in the range in which we can have only first and first and second adsorbate layers. Solid squares, 7-in-a-row solids of different densities. Solid symbols, two-layer structures with different values for the densities of 7-in-a-row solids (shown) underneath. In all cases, the second layers were translationally invariant liquid structures. The dotted line is a Maxwell construction between the stable densities of only first and first plus second layers. The error bars are the size of the symbols and are not shown for simplicity.
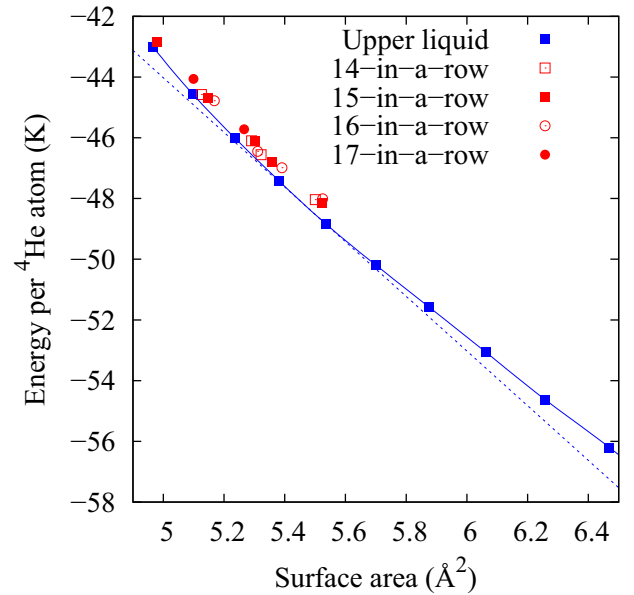
FIG. 4. Same as in Fig. 3, but for surface areas in the range of 5–6.5 Å^2. The dotted line is also the same Maxwell construction between the stable densities of only first and first plus second layers. The solid line is a guide to the eye for the results of a structure in which the second layer is a liquid. We also show simulation results for different unstable n-in-a-row second-layer solids. The error bars are the size of the symbols.

Ref. [30]; that is, we calculated the energies per particle for arrangements in which the first layers were 7-in-a-row solids with different densities with an increasing number of ^{4}He atoms placed on top. Then, the stable second layer is the one with the lowest energy for a given total density. That density is calculated as the sum of the first-layer one, in which we used as an adsorbent surface a cylinder with a radius of 6.26 Å, and the one corresponding to the second layer, computed using another cylinder whose distance from the axis of the tube was 8.98 Å. Both radii correspond to the mean distances from the atoms to the center of the tubes.

The results of the calculations for different ^{4}He loadings are displayed in Fig. 3. In Fig. 3, we can see that the lowest two-layer structure has a 7-in-a-row first-layer solid underneath with $\rho = 0.110$ Å^{-2} (solid circles) for low densities and changes to a similar structure with $\rho = 0.115$ Å^{-2} upon loading (solid squares). On the x axis we show the inverse of the density, or surface area, since in that way we can show the double-tangent Maxwell construction between a single-layer solid and the liquid on top of it. That construction, shown in Fig. 3 as a dotted line, indicates that the coexistence region is between total densities of 0.110 and 0.181 Å^{-2} (see Table I). For that last structure, the density of the solid close to the nanotube is $\rho = 0.115$ Å^{-2}. This means that, as in the case of ^{4}He adsorption on graphite, there is a compression of the layer close to the carbon when a second adsorbate sheet is deposited on top of it [30].

To see more clearly the lowest stability limit of the two-layer structure, we display in Fig. 4 a blown-up version of Fig. 3 for total surface areas in the range of 5–6.5 Å^2. The first value corresponds to the inverse of the experimental density
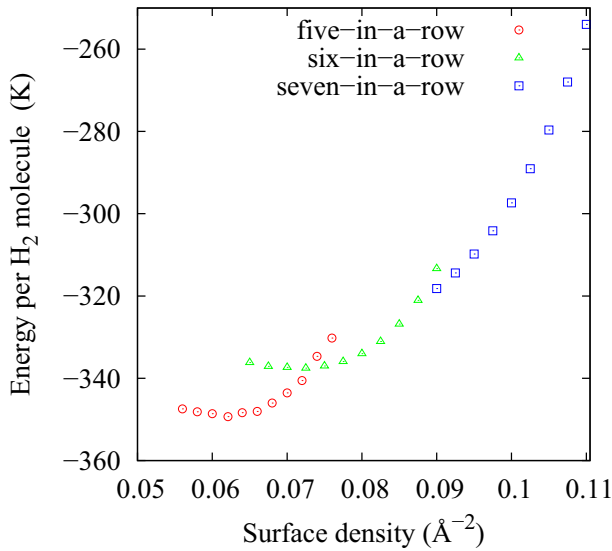
FIG. 5. Same as in Fig. 1, but for first-layer H$_2$ solids.

FIG. 6. Estimator of the superfluid density for the first-layer 5-in-a-row supersolid H$_2$ phase at $\rho = 0.062$ Å^{-2} (open squares) and for a second-layer solid at total density $\rho = 0.167$ Å^{-2} (solid squares). The straight line is a linear least-squares fit to the latter set of data for the range $\tau > 3$ K^{-1}.

for the promotion to a third layer of ^{4}He on graphite [9]. It displays the same Maxwell construction line as in Fig. 3 as a dotted line. We included also the results for several n-in-a row solid structures, with n in the range of 14–17. Those data were obtained by fixing the c_2 parameter in Eq. (3) to 0.30 Å^{-2}, but they are qualitatively similar to any simulation results in which $c_2 \neq 0$; that is, arrangements with two solid layers are always metastable with respect to others with a liquid surface on top. In this, the behavior of ^{4}He is different from that of its flat counterpart adsorbed on graphite, which solidifies before a third-layer promotion [23–26]. Obviously, that second-layer liquid is a superfluid since the value of ρ_s/ρ obtained by applying Eq. (4) is 1.

B. H$_2$

We now turn our attention to H$_2$, dealing first with first-layer solids described by Eq. (3) that do not pin the H$_2$ molecules to a single crystallographic position, as done in Ref. [16]. This opens the possibility of having supersolids, a possibility that, as we will see below, is not fulfilled.

Figure 5 is the H$_2$ counterpart of Fig. 1 for ^{4}He. The densities on the x axis are now calculated using adsorbate cylinders with a radius of 6.36 Å. This difference is due to the larger size of the H$_2$ molecule with respect to the ^{4}He atom. Making use of the double-tangent Maxwell construction lines between those solids, we find a range of densities, shown in Table I, for which we have stable 5-in-a-row and 6-in-a-row solids. In this case, contrary to what happens for ^{4}He, both the stability limits and the energies per particle are basically identical to those found in Ref. [16]. The reason can be understood by looking at Fig. 6. There, we display (open symbols) the same estimator for the superfluid density shown in Fig. 2 but for a first-layer H$_2$ solid at $\rho = 0.062$ Å^{-2}, the minimum of the 5-in-a-row energy curve in Fig. 5. We can see that $\alpha D_s(\tau)$ versus τ is constant for large τ, indicating a zero superfluid density. This means we have a first-layer normal solid as in Ref. [16]. The differences between Figs. 1 and 5 can be ascribed basically
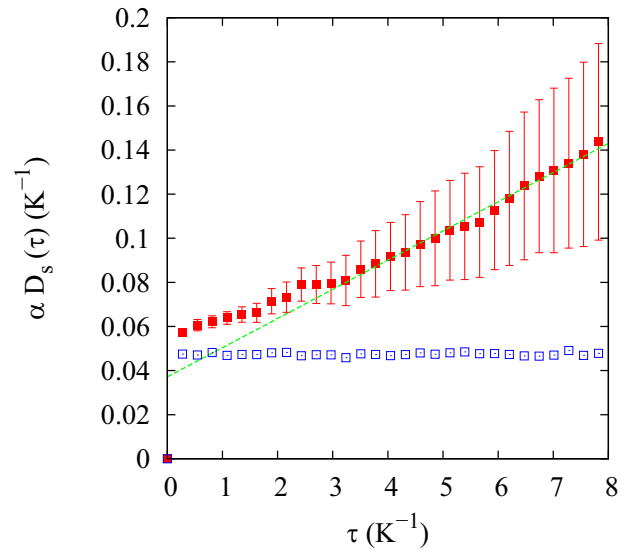
to the nature of the interparticle interactions: the larger the potential well is, the clearer the limits between the phases are.

Following exactly the same procedure as outlined above for the case of ^{4}He, we considered 7-in-a-row first-layer H$_2$ solids with different densities and deposited additional molecules on top of them. After that, we kept the arrangements with the minimum energy per particle for each total (first and second layer) density. The second-layer densities were calculated using as a surface adsorbate a cylinder with a radius of 9.42 Å. This is the mean distance of the molecules of the second layer to the axis of the tube. The minimum energies per molecule corresponded to a first-layer solid with $\rho_s = 0.100$ Å^{-2} with either a liquid [$c_2 = 0$ in Eq. (3)] or a (super)solid ($c_2 \neq 0$) on top. In Fig. 7, we show those energies as a function of the inverse of the density. The x range in Fig. 7 corresponds to the inverse of the experimental densities at which H$_2$ is short of being promoted to a third layer on a flat substrate [27]. The solid data correspond to a 15-in-a-row phase built in the same way as the first-layer solids. The dotted line is a double-tangent Maxwell construction between a single-layer 7-in-a-row solid with density $\rho = 0.0975$ Å^{-2} and a two-layer solid with total density $\rho = 0.166$ Å^{-2}. Both densities are within the error bars of the ones for a flat second H$_2$ absorbed on graphite [14].

In the same way as the second layer of H$_2$ on graphite at low densities, the 15-in-a-row H$_2$ on top of a nanotube is also a supersolid in a thin-density slice. In Fig. 6 we can see (solid squares) the same superfluid estimator already described but applied only to the molecules in the second layer for a solid with total density $\rho = 0.167$ Å^{-2}. For that arrangement, the slope corresponds to a supersolid density of $1.32\% \pm 0.05\%$, larger but of the same order of magnitude as the value for the second layer of H$_2$ on graphite ($0.41\% \pm 0.05\%$).
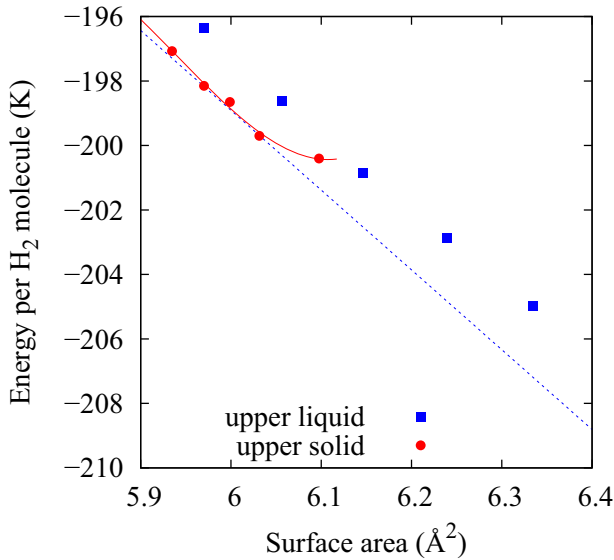
FIG. 7. Energy per H_2 molecule as a function of the inverse of the total H_2 density. Solid squares, a two-layer structure with a liquid on top of a first-layer 7-in-a-row solid of density $\rho_s = 0.100$ Å^{-2}. Solid circles, a 15-in-a-row upper solid on top of the same H_2 substrate. The dotted line is the Maxwell construction line between a single-layer solid of $\rho = 0.0975$ Å^{-2} and a two-layer solid of $\rho = 0.166$ Å^{-2}. The solid line is a third-order polynomial fit to the data intended exclusively as a guide to the eye.

IV. DISCUSSION

In this work, we have calculated the phase diagrams of ^{4}He and H_2 on a single carbon nanotube. We chose the (5,5) one because it is one of the thinnest experimentally obtained and its narrowness makes it a perfect candidate to see the differences between adsorption on a flat substrate and on a quasi-one-dimensional one. Here, the dimensionality is the only factor to take into account since the chemical compositions of graphite, graphene, and carbon nanotubes are identical. Our simulation results suggest that the behaviors of those species are quite similar on a cylinder and on its flat counterparts. There are, however, some minor differences.

^{4}He is a supersolid at low densities. In this, its behavior is similar to that of a single sheet of ^{4}He on top of graphene and graphite [12]. However, on a tube we have incommensurate structures instead of the $\sqrt{3} \times \sqrt{3}$ registered supersolid on the flat substrates. In any case, the superfluidity disappears upon ^{4}He loading: both the incommensurate solid of 0.08 Å^{-2} on graphene and the 6-in-a-row stable solids are normal. On the other hand, there is a significant difference in the promotion to a second layer. Even though on graphite there is a stable liquid in equilibrium with an incommensurate single-sheet solid, the density of that liquid is smaller than the one obtained in the present work (a total density of 0.163 Å^{-2} [13] versus a value of 0.181 Å^{-2} in Table I). In addition, we do not see a stable second-layer incommensurate solid up to the experimental density corresponding to a third-layer promotion on graphite [9].

On the other hand, the behavior of H_2 on the selected nanotube is very similar to that on top of graphene or graphite. The only difference is that, at very low densities, we have an incommensurate normal solid instead of the $\sqrt{3} \times \sqrt{3}$ normal structure on the flat adsorbents. We have also a promotion to a second-layer supersolid at the same densities as in graphite [14]. The supersolid fraction at the lowest second-layer densities is also comparable to, albeit slightly larger than, the one for graphite. This suggests that the behavior of H_2 depends more strongly on the strength of the H_2-H_2 interaction than on the dimensionality of the system and that it is probably necessary to disrupt the H_2 structure to observe new H_2 phases [31]. Another possible issue could be the quality of the empirical potential itself, and some alternatives to the Silvera-Goldman expression based on first-principles have been proposed [32–36], some of which include three-body terms. However, the equation of states of solid hcp H_2 obtained using those interactions is similar to the one calculated using the Silvera-Goldman potential [34] and in reasonable agreement with experiments. Moreover, a recent comparison between neutron scattering data for liquid and solid H_2 phases and simulations using the Silvera and Buck potentials suggested that both interactions are adequate to reproduce the experimental observables [37].

The superfluid fraction of the liquid ^{4}He layer is 1, and that of the solid H_2 layer is ∼0.01. This large difference is mainly due to the different interaction between ^{4}He atoms and H_2 molecules, the latter being much more attractive and thus favoring crystal phases. The superfluid fraction of this supersolid phase of H_2 may appear to be too small to detect, but similar fractions were experimentally measured in the second layer of ^{4}He on graphite [10] at temperatures low enough (0.5 K) to make our $T = 0$ calculations relevant. The experiment [10] was made possible by using a specially designed double torsional oscillator able to disentangle the signals coming from the superfluid and elastic responses. On the other hand, a recent calculation [38] supported the existence of supersolidity in D_2 at very high pressures.

[1] S. Iijima, Helical microtubules of graphitic carbon, Nature (London) **354**, 56 (1991).

[2] Z. Wang, J. Wei, P. Morse, J. G. Dash, O. E. Vilches, and D. H. Cobden, Phase transitions of adsorbed atoms on the surface of a carbon nanotube, Science **327**, 552 (2010).

[3] H. Lee, O. E. Vilches, Z. Wang, E. Fredrickson, P. Morse, R. Roy, D. Dzyubenko, and D. H. Cobden, Kr and ^{4}He adsorption on individual suspended single-walled carbon nanotubes, J. Low Temp. Phys. **169**, 338 (2012).

[4] H. Chiu, P. Hung, H. W. Ch. Postma, and M. Bockrath, Atomic-scale mass sensing using carbon nanotube resonators, Nano Lett. **8**, 4342 (2008).

[5] J. Chaste, A. Eichler, J. Moser, G. Ceballos, R. Rurali, and A. Bachtold, A nanomechanical mass sensor with yoctogram resolution, Nat. Nanotechnol. **7**, 301 (2012).

[6] A. Tavernarakis, J. Chaste, A. Eichler, G. Ceballos, M. C. Gordillo, J. Boronat, and A. Bachtold, Atomic Monolayer Deposition on the Surface of Nanotube Mechanical Resonators, Phys. Rev. Lett. **112**, 196103 (2014).

[7] A. Noury, J. Vergara-Cruz, P. Morfin, B. Plaçais, M. C. Gordillo, J. Boronat, S. Balibar, and A. Bachtold, Layering Transition in Superfluid Helium Adsorbed on a Carbon Nanotube Mechanical Resonator, Phys. Rev. Lett. **122**, 165301 (2019).

[8] I. Todoshchenko, M. Kamada, J. P. Kaikkonen, Y. Liao, A. Savin, M. Will, E. Sergeicheva, T. S. Abhilash, E. Kauppinen, and P. Hakonen, Topologically-imposed vacancies and mobile solid ^{3}He on carbon nanotube, Nat. Commun. **13**, 5873 (2022).

[9] J. Nyeki, A. Phillis, A. Ho, D. Lee, P. Coleman, J. Parpia, B. Cowan, and J. Saunders, Intertwined superfluid and density wave order in two-dimensional ^{4}He, Nat. Phys. **13**, 455 (2017).

[10] J. Choi, A. A. Zadorozhko, J. Choi, and E. Kim, Spatially Modulated Superfluid State in Two-Dimensional ^{4}He Films, Phys. Rev. Lett. **127**, 135301 (2021).

[11] S. Nakamura, K. Matsui, T. Matsui, and H. Fukuyama, Possible quantum liquid crystal phases of helium monolayers, Phys. Rev. B **94**, 180501(R) (2016).

[12] M. C. Gordillo, C. Cazorla, and J. Boronat, Supersolidity in quantum films adsorbed on graphene and graphite, Phys. Rev. B **83**, 121406(R) (2011).

[13] M. C. Gordillo and J. Boronat, Superfluid and Supersolid Phases of ^{4}He on the Second Layer of Graphite, Phys. Rev. Lett. **124**, 205301 (2020).

[14] M. C. Gordillo and J. Boronat, Supersolidity in the second layer of para-H$_2$ adsorbed on graphite, Phys. Rev. B **105**, 094501 (2022).

[15] M. C. Gordillo and J. Boronat, ^{4}He adsorbed outside a single carbon nanotube, Phys. Rev. B **86**, 165409 (2012).

[16] M. C. Gordillo and J. Boronat, Phase transitions of H$_2$ adsorbed on the surface of single carbon nanotubes, Phys. Rev. B **84**, 033406 (2011).

[17] W. Carlos and M. W. Cole, Interaction between a He atom and a graphite surface, Surf. Sci. **91**, 339 (1980).

[18] G. Stan and M. W. Cole, Hydrogen adsorption in nanotubes, J. Low Temp. Phys. **110**, 539 (1998).

[19] F. M. R. A. Aziz and C. K. Wong, A new determination of the ground state interatomic potential for He$_2$, Mol. Phys. **61**, 1487 (1987).

[20] I. F. Silvera and V. V. Goldman, The isotropic intermolecular potential for H$_2$ and D$_2$ in the solid and gas phases, J. Chem. Phys. **69**, 4209 (1978).

[21] M. C. Gordillo and J. Boronat, ^{4}He on a Single Graphene Sheet, Phys. Rev. Lett. **102**, 085303 (2009).

[22] M. C. Gordillo and J. Boronat, Phase diagram of H$_2$ adsorbed on graphene, Phys. Rev. B **81**, 155435 (2010).

[23] P. A. Crowell and J. D. Reppy, Reentrant Superfluidity in ^{4}He Films Adsorbed on Graphite, Phys. Rev. Lett. **70**, 3291 (1993).

[24] P. A. Crowell and J. D. Reppy, Superfluidity and film structure in ^{4}He adsorbed on graphite, Phys. Rev. B **53**, 2701 (1996).

[25] D. S. Greywall and P. A. Busch, Heat Capacity of Fluid Monolayers of ^{4}He, Phys. Rev. Lett. **67**, 3535 (1991).

[26] D. S. Greywall, Heat capacity and the commensurate-incommensurate transition of ^{4}He adsorbed on graphite, Phys. Rev. B **47**, 309 (1993).

[27] H. Wiechert, Thermodynamic and neutron-diffraction studies of H$_2$ and D$_2$ multilayers physisorbed on graphite, in *Excitations in Two-Dimensional and Three-Dimensional Quantum Fluid*, edited by A. Wyatt and H. Lauter (Plenum, New York, 1991), p. 499.

[28] M. C. Gordillo and J. Boronat, Second layer of H$_2$ and D$_2$ adsorbed on graphene, Phys. Rev. B **87**, 165403 (2013).

[29] S. Zhang, N. Kawashima, J. Carlson, and J. E. Gubernatis, Quantum Simulations of the Superfluid-Insulator Transition for Two-Dimensional, Disordered, Hard-Core Bosons, Phys. Rev. Lett. **74**, 1500 (1995).

[30] M. C. Gordillo and J. Boronat, Zero-temperature phase diagram of the second layer of ^{4}He adsorbed on graphene, Phys. Rev. B **85**, 195457 (2012).

[31] M. C. Gordillo and J. Boronat, H$_2$ superglass on an amorphous carbon substrate, Phys. Rev. B **107**, L060505 (2023).

[32] N. Faruk, M. Schmidt, H. Li, R. J. Le Roy, and P. Roy, First-principles prediction of the raman shifts in parahydrogen clusters, J. Chem. Phys. **141**, 014310 (2014).

[33] M. Schmidt, J. M. Fernández, N. Faruk, M. Nooijen, R. J. Le Roy, J. H. Morilla, G. Tejeda, S. Montero, and P. Roy, Raman vibrational shifts of small clusters of hydrogen isotopologues, J. Phys. Chem. A **119**, 12551 (2015).

[34] A. Ibrahim, L. Wang, T. Halverson, R. J. Le Roy, and P. Roy, Equation of state and first principles prediction of the vibrational matrix shift of solid parahydrogen, J. Chem. Phys. **151**, 244501 (2019).

[35] A. Ibrahim and P. Roy, Three-body potential energy surface for para-hydrogen, J. Chem. Phys. **156**, 044301 (2022).

[36] A. Ibrahim and P. Roy, Equation of state of solid parahydrogen using ab initio two-body and three-body interaction potentials, J. Chem. Phys. **157**, 174503 (2022).

[37] T. R. Prisk, R. T. Azuah, D. L. Abernathy, G. E. Granroth, T. E. Sherline, P. E. Sokol, J. Hu, and M. Boninsegni, Zero-point motion of liquid and solid hydrogen, Phys. Rev. B **107**, 094511 (2023).

[38] C. W. Myung, B. Hirshberg, and M. Parrinello, Prediction of a Supersolid Phase in High-Pressure Deuterium, Phys. Rev. Lett. **128**, 045301 (2022).